PHYSICAL REVIEW LETTERS **129,** 050503 (2022)

Editors' Suggestion **Featured in Physics**

Postselected Entanglement between Two Atomic Ensembles Separated by 12.5 km

Xi-Yu Luo,[1,2,3] Yong Yu,[1,2,3] Jian-Long Liu,[1,2,3] Ming-Yang Zheng,[4] Chao-Yang Wang,[1,2,3] Bin Wang,[1,2,3] Jun Li,[1,2,3]
Xiao Jiang,[1,2,3] Xiu-Ping Xie,[4] Qiang Zhang,[1,2,3,4] Xiao-Hui Bao,[1,2,3] and Jian-Wei Pan[1,2,3]
[1]*Hefei National Research Center for Physical Sciences at the Microscale and School of Physical Sciences,*
University of Science and Technology of China, Hefei 230026, China
[2]*CAS Center for Excellence in Quantum Information and Quantum Physics,*
University of Science and Technology of China, Hefei 230026, China
[3]*Hefei National Laboratory, University of Science and Technology of China, Hefei 230088, China*
[4]*Jinan Institute of Quantum Technology, Jinan 250101, China*

(Received 1 April 2022; accepted 14 June 2022; published 28 July 2022)

Quantum internet gives the promise of getting all quantum resources connected, and it will enable applications far beyond a localized scenario. A prototype is a network of quantum memories that are entangled and well separated. In this Letter, we report the establishment of postselected entanglement between two atomic quantum memories physically separated by 12.5 km directly. We create atom-photon entanglement in one node and send the photon to a second node for storage via electromagnetically induced transparency. We harness low-loss transmission through a field-deployed fiber of 20.5 km by making use of frequency down-conversion and up-conversion. The final memory-memory entanglement is verified to have a fidelity of 90% via retrieving to photons. Our experiment makes a significant step forward toward the realization of a practical metropolitan-scale quantum network.

DOI: 10.1103/PhysRevLett.129.050503

Quantum memory is an essential element in a quantum network [1,2], since it mediates the photonic qubit transmissions and the matter qubit manipulations. A prototype of quantum networks is the entanglement of well-separated quantum memories. Experimentally, two-node entanglement has been realized through various approaches, such as solid-state impurities [3], quantum dots [4], trapped ions [5] and neutral atoms [6,7], cold atomic ensembles [8], and rare-earth ion ensembles [9,10]. Extension to three nodes was also reported recently [11,12]. Moving from these proof-of-principle experiments to a genuine quantum network in the metropolitan regime is not only indispensable for the promising applications (such as device-independent quantum key distribution [13–16], deterministic quantum teleportation [17,18], quantum repeater [19], distributed quantum computing [7,20,21], entanglement-based clock synchronization [22]), but also significantly meaningful for the test of quantum foundations [3,23]. Extension to longer distance is facing a number of challenges. One major limiting issue is that the photon wavelength of most memories is not suitable for low-loss transmission in optical fibers; thus, an efficient and low-noise quantum frequency converter (QFC) [24–31] is required. Another issue is that the two nodes need to be fully independent, which raises experimental complexities [8] involving remote phase synchronization, etc. In addition, the memory needs to be long-lived with a lifetime significantly longer than the fiber transmission delay.

Here, we resolve these issues by reporting the establishment of entanglement between two quantum memories that are fully independent and long-distance separated. We make use of two quantum memory nodes separated by 12.5 km physically and connected with optical fibers of 20.5 km. The memories are based on laser-cooled atomic ensembles, for which key capabilities have been realized already, such as subsecond storage [32,33], efficient retrieval [11,32–36], and spatial [37,38] and temporal [39] multiplexing. In one node, we design a scheme to directly generate entanglement of the atomic ensemble with a single photon in the time-bin degree. The atomic coherence is prolonged via zeroing the spin-wave wave vector. By transmitting the photon to the other node and storing it, we entangle the two remote quantum memories. The transmitted photon is shifted in frequency from the rubidium D_1 line to the O band in fiber-optic communication to minimize the transmission losses [8]. Working in the time-bin degree not only enhances the robustness of long-distance transmission, but also simplifies the design of the frequency conversion modules significantly. The final memory-memory entanglement is postselectively verified via retrieving to photons, giving a fidelity of 90%. Further incorporating heralded storage [40,41], the success of remote entanglement will become heralded and enable the study of quantum network applications [2] in a practical scenario.

The layout of our experiment is shown in Fig. 1. It comprises two nodes distantly separated in Hefei city,

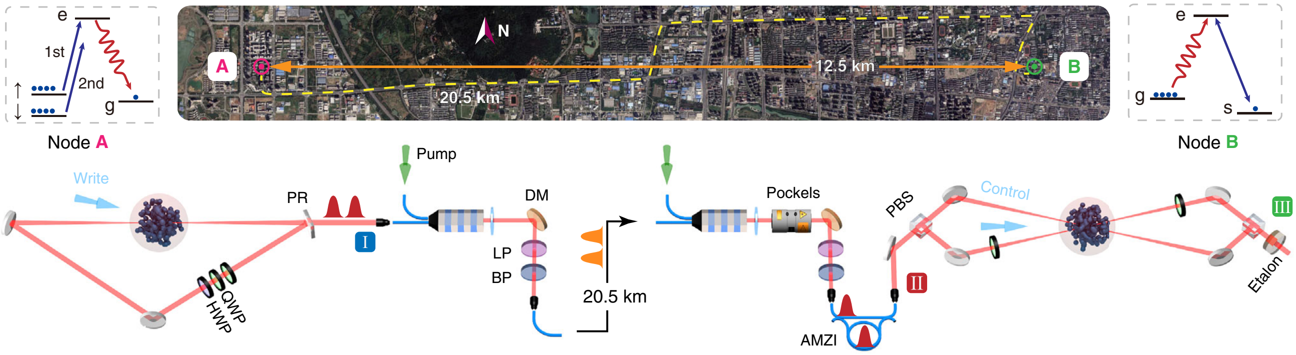

FIG. 1. Experimental layout. Bird's eye view (top) of the memory nodes (A and B) that are 12.5 km apart and connected with fibers of 20.5 km (17 km deployed together with a 3.5 km long fiber loop). Each node includes a setup with ^{87}Rb atoms and a quantum frequency converter. Schematic (bottom) and corresponding level schemes (insets). In node A, a cavity-enhanced DLCZ-type setup is used to generate atom-photon entanglement. The write-out photon propagates along the clockwise mode of the cavity and emits from the partially reflective mirror (PR). The emitted photon is then converted to 1342 nm via DFG in a PPLN waveguide and transmitted to node B via the fiber channel. In node B, the photon is first converted back to 795 nm via SFG in another PPLN waveguide chip. A series of filters, including dichroic mirrors (DM), long-pass filters (LP), and bandpass filters (BP), are used to suppress the noise in each conversion module. (The types and quantities shown in the figure are not in one to one correspondence with the actual situation). The photon's two time-bin modes are then converted to two spatial modes and stored in the atomic ensemble by applying a control pulse via the EIT mechanism. The time-bin to spatial conversion is achieved by a combination of a Pockels cell, an asymmetric Mach-Zehnder interferometer (AMZI), and a polarizing beam splitter (PBS). An etalon in the readout path of the EIT quantum memory is for blocking the control pulse leakage. QWP and HWP are quarter- and half-wave plates, respectively. Markers I, II, and III indicate three checkpoints for the write-out photon during the characterization of the photon transfer and the EIT storage. Map data is from Google and Maxar Technologies.

labeled as A and B, and several field-deployed optical fibers linking them. We start by generating atom-photon time-bin entanglement in node A using an improved version of the Duan-Lukin-Cirac-Zoller (DLCZ) scheme [42]. A laser-cooled ^{87}Rb atomic ensemble is initially prepared as a mixture of $|\downarrow\rangle$ and $|\uparrow\rangle$, two Zeeman levels of the lowest atomic hyperfine ground state $|g\rangle \equiv |5S_{1/2}, F = 1\rangle$ with the magnetic quantum number $m_F = -1$ and $+1$, respectively (see Supplemental Material [43]). Two write pulses with orthogonal polarizations drive spontaneous Raman scattering from $|\downarrow\rangle$ and $|\uparrow\rangle$ in sequence. In a small probability χ, a write-out photon is scattered along the ring cavity mode through the early process along with a spin wave $|\Downarrow\rangle = \sum_j e^{i\Delta\vec{k}\cdot\vec{r}_j}|\downarrow \ldots s_j \ldots \downarrow\rangle$, or through the late process along with another spin wave $|\Uparrow\rangle = \sum_j e^{i\Delta\vec{k}\cdot\vec{r}_j}|\uparrow \ldots s_j \ldots \uparrow\rangle$, where $\Delta\vec{k}$ is the wave vector difference of write beam and write-out photon, also known as the wave vector of the spin wave. These two spin-wave states form an atomic qubit. Ensuring coherence between two write pulses, we generate a maximally entangled atom-photon state,

$$|\Psi_{\mathrm{ap}}\rangle = \frac{1}{\sqrt{2}}(|\Downarrow\rangle|E\rangle + e^{-i\varphi(t)}|\Uparrow\rangle|L\rangle), \tag{1}$$

where E and L denote the write-out photon's early and late time-bin mode, respectively. A time-dependent phase $\varphi(t) = \mu_B B t/\hbar + \varphi_0$ is involved due to the Zeeman splitting induced by a bias magnetic field B, where μ_B is the Bohr magneton, $\hbar$ is the reduced Planck constant, and t is the evolution time. Besides being intrinsically appropriate for long-distance transmission, the time-bin encoded photon is favorable for the following QFC process for avoiding polarization selection of nonlinear process. Two spin-wave modes can be efficiently retrieved on demand as two orthogonal polarization photon modes for measurement. Write-out photons are next down-converted from rubidium resonance to telecom O band to minimize the transmission attenuation. This is achieved by the difference frequency generation (DFG) process in a periodically poled lithium niobate (PPLN) waveguide chip with the help of a strong 1950 nm pump laser.

At node B, the telecom photon is up-converted back to 795 nm with the help of the sum-frequency generation (SFG) process in another PPLN waveguide chip to match the rubidium resonance. Before the SFG process, we compensate the fiber-induced polarization drift by continuously adjusting an electrical polarization controller [8]. In this node, another laser-cooled ^{87}Rb atomic ensemble initialized in $|a\rangle \equiv |5S_{1/2}, F = 2, m_F = +2\rangle$ serves as the quantum memory. By applying a strong control field coupling a stable state $|b\rangle \equiv |5S_{1/2}, F = 1, m_F = 0\rangle$ with an excited state $|c\rangle \equiv |5P_{1/2}, F = 1, m_F = +1\rangle$, the input photon on resonance with $|a\rangle \leftrightarrow |c\rangle$ is mapped as a spin wave $\sum_i |a \ldots c_i \ldots a\rangle$ through the electromagnetically induced transparency (EIT) [44]. Two time-bin modes, $|E\rangle$ and $|L\rangle$, of the input photon are transformed to two spatial modes up and down, respectively, and stored afterward. In this way, we create a remote atom-atom entanglement,

$$|\Psi_{\mathrm{aa}}\rangle = \frac{1}{\sqrt{2}}(|\Downarrow\rangle|U\rangle + e^{-i\varphi(t)}|\Uparrow\rangle|D\rangle), \tag{2}$$

where $|U\rangle$ and $|D\rangle$ denote two spin-wave states of up and down spatial mode, respectively.

Entanglement distribution between distant network nodes can be extremely time-consuming, which raises a critical demand for long-lived storage. In this experiment, it is essential that the quantum memory at node A can survive longer than the communication time of 103 μs between the two nodes. A dominant decoherence mechanism for spin waves in the atomic ensemble is the thermal motion $\vec{r}_j' = \vec{v}_j t$ of atoms. It will introduce a random phase $\Delta\vec{k}\cdot\vec{r}_j{}'$ to each item and ruin the collective interference process during retrieval. Here, by making use of an auxiliary state $|s'\rangle \equiv |5^2S_{1/2}, F=2, m_F=-1\rangle$, we coherently freeze the spin wave [45] to minimize the thermal motion-induced decoherence as shown in Fig. 2(a). Two Raman beams driving the atom from $|s\rangle$ to $|s'\rangle$ with a π transition will kick the atom with a momentum of $\hbar\vec{k}_R$, leading to an engineered wave vector $\Delta\vec{k}' = \Delta\vec{k} + \vec{k}_R$, where $\vec{k}_R$ is the difference between the wave vector of two Raman beams. With an appropriate arrangement of Raman beams, $|\Delta\vec{k}'|$ is minimized to a near-zero value (see Supplemental Material [43]). Note that the engineering process works for both spin-wave modes since their initial wave vectors are identical. We observed a $1/e$ lifetime of 416 μs and 517 μs for $|\Downarrow\rangle$ and $|\Uparrow\rangle$, respectively, as shown in Fig. 2(b), both surpassing the entanglement distribution time in this experiment. A slightly longer lifetime of $|\Uparrow\rangle$ originates from its magnetic field insensitive clock-state energy level configuration during the spin-wave freezing.

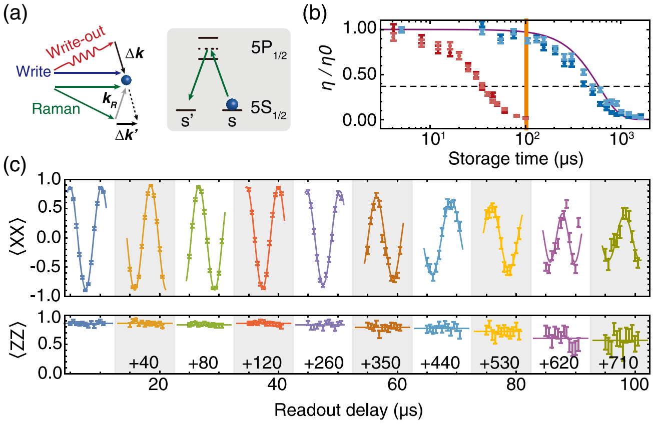

FIG. 2. Benchmarking the DLCZ quantum memory. (a) Scheme of the spin-wave freezing. After the spin wave was created, a Raman π pulse that couples the $|s\rangle$ to $|s'\rangle$ transition via a two-photon Raman process is applied. The Raman process introduces a new momentum $\hbar\vec{k}_R$ to the $|s\rangle/|s'\rangle$ state atom, resulting in an altered spin wave with the wave vector $\Delta\vec{k}' = \Delta\vec{k} + \vec{k}_R \approx 0$. The Raman π pulse is applied again before the readout to recover the wave vector. (b) Relative retrieval efficiency (η/η_0) as a function of the readout delay. The data for two spin-wave states are dark and light blue for the spin-wave freezing case and dark and light red for the spin-wave freezing free case. The purple curve is the theoretical expectation of the spin-wave freezing (see Supplemental Material [43]). The orange bar indicates the entanglement distribution time in the experiment. (c) Measured atom-photon correlations at $\chi = 5.4\%$ as a function of the readout delay. The oscillation of $\langle XX\rangle$ originates from the time evolution of the atomic phase induced by the magnetic field. Error bars indicate one standard deviation of the photon-counting statistics.

As the atomic qubit in node A is phase-evolving under the bias magnetic field, its coherence relies on the stability of the magnetic field. Thus, we take passive and active measures to cancel magnetic noise (see Supplemental Material [43]). To characterize the coherence of the atomic qubit, we prepare an entangled state as in Eq. (1) and measure the atom-photon correlation in XX and ZZ basis along with the storage time increase [Fig. 2(c)], where hereafter we use X, Y, and Z as the shorthand for standard Pauli matrices σ_x, σ_y, and σ_z, respectively, for both atomic and photonic qubits. We can observe an oscillation under XX basis caused by the time-evolving phase. By fitting the decrease of $\langle ZZ\rangle$ and the envelope of $\langle XX\rangle$, we deduce an average amplitude damping time $T_1 = 1.2$ ms and a phase damping time $T_2^* = 856.7$ μs for qubit storage.

Next, we investigate the photon state transfer between two nodes. The optimal end-to-end efficiency for DFG and SFG modules is 46% and 45%, respectively. Together with the 7.1 dB transmission losses of the fiber channel, we have a photon transfer efficiency from node A to B around 4%. As a comparison, the transmission efficiency of a 795 nm photon on the same fiber channel without frequency conversion will be on the order of 10^{-7}. The EIT memory used is similar to the one used in our previous publication [46], which has a memory lifetime around 57 μs. The storage efficiency, including mapping in and mapping out, is about 22% and 25% for two spatial modes $|D\rangle$ and $|U\rangle$, respectively. The imbalance in storage efficiency compensates the imbalance in transmission efficiency through the AMZI (67% and 76% for $|E\rangle$ and $|L\rangle$, respectively). Noise photons introduced during the photon transfer and storage will lead to depolarization of the remote entanglement. To determine the noise strength, by setting $\chi = 5.4\%$, we measure the signal-to-noise ratio (SNR) of the write-out photon at three different checkpoints, namely, before transfer at I, after transfer at II, and after storage and readout in the EIT quantum memory at III (see labels in Fig. 1) as shown in Fig. 3(a). Thanks to the efficient noise filtering during QFC, the SNR hardly drops as the photon propagates from I to II. The obvious decrease of the SNR after EIT storage is due to a reduced signal strength that is approaching the dark counts level of the silicon-based

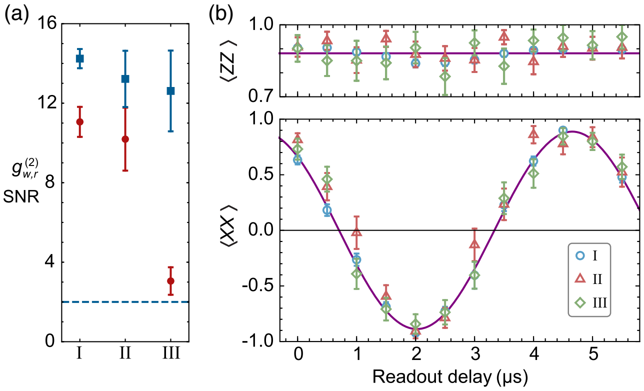

FIG. 3. Characterization of the photon transfer and the EIT quantum memory. (a) Red dots shows the measured SNR of the write-out photon before transfer (I), after transfer (II), and after EIT storage (III). The normalized cross-correlation function $g^{(2)}_{w,r}$ between the write-out and the read-out photon at the corresponding three conditions are shown in blue squares. (b) Measured $\langle ZZ\rangle$ and $\langle XX\rangle$ correlations of $|\Psi_{\mathrm{ap}}\rangle$ as a function of readout delay, i.e., the atomic phase evolution. Blue circles, red triangle, and green diamond refer to measuring the write-out photon at I, II, and III. The purple curve in each graph shows the fitting for data in case I. Error bars indicate one standard deviation of the photon-counting statistics.

single-photon detectors, which can be drastically mitigated by using superconducting nanowire single-photon detectors with ultralow dark counts [47]. Nevertheless, the strong atom-photon correlation barely suffers from the noise. As also depicted in Fig. 3(a), we observed a uniformed cross-correlation function between the write-out and the read-out photon $g^{(2)}_{w,r}$ of 13.2 ± 1.4 and 12.6 ± 2.0 when measuring the write-out photon at II and III, respectively, which are slightly lower than the initial value 14.2 ± 0.5 when measuring the write-out photon at I. We also measured the atom-photon correlation under different Pauli basis at these checkpoints [Fig. 3(b)]. When sweeping the readout delay, i.e., the entanglement phase $\varphi(t)$, strong and near-identical correlation variation for $\langle XX\rangle$ and $\langle ZZ\rangle$ for the three checkpoints reveals a high-quality photon transfer and EIT storage. The atomic state for all cases is measured within $5\ \mu s$ ($\ll T_1, T_2^*$) after the entanglement was created to get rid of the influence from time-dependent dephasing.

Finally, we run the full entangling scheme and verify the entanglement when it evolves to a Bell state $|\Psi^+_{\mathrm{aa}}\rangle = (|\Downarrow\rangle|U\rangle + |\Uparrow\rangle|D\rangle)/\sqrt{2}$. We first measure the S parameter in the Clauser-Horne-Shimony-Holt–type Bell inequality,

$$S = |\langle A_0 \times B_0\rangle + \langle A_0 \times B_1\rangle + \langle A_1 \times B_0\rangle - \langle A_1 \times B_1\rangle|.$$

For node A, two observables A_0 and A_1 are Z and X, respectively, and for node B, two observables B_0 and B_1 are

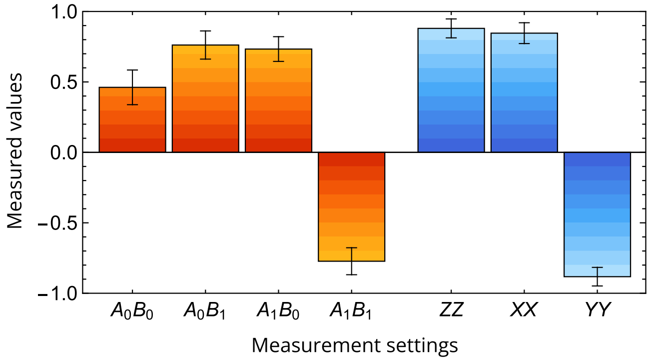

FIG. 4. Two-node entanglement. Results of the Bell test and the correlation measurement with the remote atom-atom entanglement $|\Psi^+_{\mathrm{aa}}\rangle$. Error bars indicate one standard deviation of the photon-counting statistics.

$(-Z + X)/\sqrt{2}$ and $(-Z - X)/\sqrt{2}$, respectively. Results for four settings are shown in Fig. 4. We obtain $S = 2.73 \pm 0.20$, which violates the classical bound of $S \leq 2$ by more than 3 standard deviations. To qualify the entanglement more quantitatively, we measure its fidelity with respect to the target state $|\Psi^+_{\mathrm{aa}}\rangle$ as

$$\mathcal{F} = \mathrm{Tr}(|\Psi^+_{\mathrm{aa}}\rangle\langle\Psi^+_{\mathrm{aa}}|\rho) = \frac{1}{4}(1 + \langle XX\rangle - \langle YY\rangle + \langle ZZ\rangle).$$

Figure 4 summarizes the observed data and we find $\mathcal{F} = 0.90 \pm 0.03$. This fidelity considerably exceeds the threshold of $\mathcal{F} > 0.5$ to witness entanglement for a Bell state and step into the regime for practical applications [2].

The overall atom-atom entangling efficiency in each trial is 0.03%, including the write-out photon generation efficiency and coupling efficiency, DFG efficiency, fiber transmission efficiency, SFG efficiency, and the EIT mapping-in efficiency. One main limitation lies in the process of atom-photon entanglement generation in node A, since it is intrinsically probabilistic. Exciting the atomic ensemble with write pulses of higher intensity will increase the write-out photon generation efficiency, but simultaneously leads to more contribution from higher-order events and gets entanglement fidelity reduced. One solution is making use of a deterministic scheme of entanglement generation via Rydberg blockade [48]. Through optical engineering and optimization, harnessing an atomic ensemble with a very high optical depth for node B, one may push the overall entangling efficiency toward a pure fiber attenuation. Currently, the success of remote entanglement is postselected via the photon detection at node B, which may give some limitations for potential applications. A better choice will be using a heralded quantum memory [40,41] for node B instead, which will extend the range of applications significantly. Since the SNR at node B is mainly limited by detector dark counts, adoption of heralded storage with a similar efficiency as our EIT memory will improve the SNR as well. The remote entanglement fidelity in our experiment is mainly limited by the high-order events in node A. Adopting a deterministic scheme with Rydberg atoms will shift this problem to improving the precision of the Rydberg-state manipulations. Our experiment demonstrates the very elementary process of quantum networking at the metropolitan scale, and adoption of similar techniques in a multinode configuration [11,12] will enable functionalities significantly beyond a two-node scenario.

This work was supported by National Key R&D Program of China (Nos. 2017YFA0303902, 2020YFA 0309804), Anhui Initiative in Quantum Information Technologies, National Natural Science Foundation of China, and the Chinese Academy of Sciences. We acknowledge QuantumCTek for the allocation of node A.

X.-Y. L. and Y. Y. contributed equally to this work.

Note added.—During the preparation of this manuscript, we became aware of a related experiment [49] that realizes entanglement of two single atoms separated by 400 m with a fiber length of 33 km.

---

[1] H. J. Kimble, Nature (London) **453**, 1023 (2008).
[2] S. Wehner, D. Elkouss, and R. Hanson, Science **362**, eaam9288 (2018).
[3] B. Hensen, H. Bernien, A. E. Dréau, A. Reiserer, N. Kalb, M. S. Blok, J. Ruitenberg, R. F. L. Vermeulen, R. N. Schouten, C. Abellán, W. Amaya, V. Pruneri, M. W. Mitchell, M. Markham, D. J. Twitchen, D. Elkouss, S. Wehner, T. H. Taminiau, and R. Hanson, Nature (London) **526**, 682 (2015).
[4] A. Delteil, Z. Sun, W.-b. Gao, E. Togan, S. Faelt, and A. Imamoğlu, Nat. Phys. **12**, 218 (2016).
[5] D. Hucul, I. V. Inlek, G. Vittorini, C. Crocker, S. Debnath, S. M. Clark, and C. Monroe, Nat. Phys. **11**, 37 (2015).
[6] J. Hofmann, M. Krug, N. Ortegel, L. Gerard, M. Weber, W. Rosenfeld, and H. Weinfurter, Science **337**, 72 (2012).
[7] S. Daiss, S. Langenfeld, S. Welte, E. Distante, P. Thomas, L. Hartung, O. Morin, and G. Rempe, Science **371**, 614 (2021).
[8] Y. Yu, F. Ma, X.-Y. Luo, B. Jing, P.-F. Sun, R.-Z. Fang, C.-W. Yang, H. Liu, M.-Y. Zheng, X.-P. Xie, W.-J. Zhang, L.-X. You, Z. Wang, T.-Y. Chen, Q. Zhang, X.-H. Bao, and J.-W. Pan, Nature (London) **578**, 240 (2020).
[9] D. Lago-Rivera, S. Grandi, J. V. Rakonjac, A. Seri, and H. de Riedmatten, Nature (London) **594**, 37 (2021).
[10] X. Liu, J. Hu, Z.-F. Li, X. Li, P.-Y. Li, P.-J. Liang, Z.-Q. Zhou, C.-F. Li, and G.-C. Guo, Nature (London) **594**, 41 (2021).
[11] B. Jing, X.-J. Wang, Y. Yu, P.-F. Sun, Y. Jiang, S.-J. Yang, W.-H. Jiang, X.-Y. Luo, J. Zhang, X. Jiang, X.-H. Bao, and J.-W. Pan, Nat. Photonics **13**, 210 (2019).
[12] M. Pompili, S. L. N. Hermans, S. Baier, H. K. C. Beukers, P. C. Humphreys, R. N. Schouten, R. F. L. Vermeulen, M. J. Tiggelman, L. d. S. Martins, B. Dirkse, S. Wehner, and R. Hanson, Science **372**, 259 (2021).
[13] D. Mayers and A. Yao, in *Proceedings 39th Annual Symposium on Foundations of Computer Science (Cat. No. 98CB36280)* (IEEE, New York, 1998), pp. 503–509, 10.1109/SFCS.1998.743501.
[14] J. Barrett, L. Hardy, and A. Kent, Phys. Rev. Lett. **95**, 010503 (2005).
[15] A. Acín, N. Brunner, N. Gisin, S. Massar, S. Pironio, and V. Scarani, Phys. Rev. Lett. **98**, 230501 (2007).
[16] S. Pironio, A. Acín, N. Brunner, N. Gisin, S. Massar, and V. Scarani, New J. Phys. **11**, 045021 (2009).
[17] W. Pfaff, B. J. Hensen, H. Bernien, S. B. van Dam, M. S. Blok, T. H. Taminiau, M. J. Tiggelman, R. N. Schouten, M. Markham, D. J. Twitchen, and R. Hanson, Science **345**, 532 (2014).
[18] S. Langenfeld, S. Welte, L. Hartung, S. Daiss, P. Thomas, O. Morin, E. Distante, and G. Rempe, Phys. Rev. Lett. **126**, 130502 (2021).
[19] H.-J. Briegel, W. Dür, J. I. Cirac, and P. Zoller, Phys. Rev. Lett. **81**, 5932 (1998).
[20] C. Monroe, R. Raussendorf, a. Ruthven, K. R. Brown, P. Maunz, L.-M. Duan, and J. Kim, Phys. Rev. A **89**, 022317 (2014).
[21] K. S. Chou, J. Z. Blumoff, C. S. Wang, P. C. Reinhold, C. J. Axline, Y. Y. Gao, L. Frunzio, M. Devoret, L. Jiang, and R. Schoelkopf, Nature (London) **561**, 368 (2018).
[22] P. Kómár, E. M. Kessler, M. Bishof, L. Jiang, A. S. Sørensen, J. Ye, and M. D. Lukin, Nat. Phys. **10**, 582 (2014).
[23] W. Rosenfeld, D. Burchardt, R. Garthoff, K. Redeker, N. Ortegel, M. Rau, and H. Weinfurter, Phys. Rev. Lett. **119**, 010402 (2017).
[24] A. G. Radnaev, Y. O. Dudin, R. Zhao, H. H. Jen, S. D. Jenkins, A. Kuzmich, and T. a. B. Kennedy, Nat. Phys. **6**, 894 (2010).
[25] N. Maring, P. Farrera, K. Kutluer, M. Mazzera, G. Heinze, and H. de Riedmatten, Nature (London) **551**, 485 (2017).
[26] K. De Greve, L. Yu, P. L. McMahon, J. S. Pelc, C. M. Natarajan, N. Y. Kim, E. Abe, S. Maier, C. Schneider, M. Kamp, S. Höfling, R. H. Hadfield, A. Forchel, M. M. Fejer, and Y. Yamamoto, Nature (London) **491**, 421 (2012).
[27] M. Bock, P. Eich, S. Kucera, M. Kreis, A. Lenhard, C. Becher, and J. Eschner, Nat. Commun. **9**, 1998 (2018).
[28] R. Ikuta, T. Kobayashi, T. Kawakami, S. Miki, M. Yabuno, T. Yamashita, H. Terai, M. Koashi, T. Mukai, T. Yamamoto, and N. Imoto, Nat. Commun. **9**, 1997 (2018).
[29] T. van Leent, M. Bock, R. Garthoff, K. Redeker, W. Zhang, T. Bauer, W. Rosenfeld, C. Becher, and H. Weinfurter, Phys. Rev. Lett. **124**, 010510 (2020).
[30] A. Tchebotareva, S. L. N. Hermans, P. C. Humphreys, D. Voigt, P. J. Harmsma, L. K. Cheng, A. L. Verlaan, N. Dijkhuizen, W. de Jong, A. Dréau, and R. Hanson, Phys. Rev. Lett. **123**, 063601 (2019).
[31] V. Krutyanskiy, M. Meraner, J. Schupp, V. Krcmarsky, H. Hainzer, and B. P. Lanyon, npj Quantum Inf. **5**, 72 (2019).
[32] S.-J. Yang, X.-J. Wang, X.-H. Bao, and J.-W. Pan, Nat. Photonics **10**, 381 (2016).
[33] X.-J. Wang, S.-J. Yang, P.-F. Sun, B. Jing, J. Li, M.-T. Zhou, X.-H. Bao, and J.-W. Pan, Phys. Rev. Lett. **126**, 090501 (2021).

[34] Y.-W. Cho, G. T. Campbell, J. L. Everett, J. Bernu, D. B. Higginbottom, M. T. Cao, J. Geng, N. P. Robins, P. K. Lam, and B. C. Buchler, Optica **3**, 100 (2016).

[35] Y. Wang, J. Li, S. Zhang, K. Su, Y. Zhou, K. Liao, S. Du, H. Yan, and S.-L. Zhu, Nat. Photonics **13**, 346 (2019).

[36] M. Cao, F. Hoffet, S. Qiu, A. S. Sheremet, and J. Laurat, Optica **7**, 1440 (2020).

[37] Y.-F. Pu, N. Jiang, W. Chang, H.-X. Yang, C. Li, and L.-M. Duan, Nat. Commun. **8**, 1 (2017).

[38] R. Chrapkiewicz, M. Dabrowski, and W. Wasilewski, Phys. Rev. Lett. **118**, 063603 (2017).

[39] L. Heller, P. Farrera, G. Heinze, and H. de Riedmatten, Phys. Rev. Lett. **124**, 210504 (2020).

[40] H. Tanji, S. Ghosh, J. Simon, B. Bloom, and V. Vuletić, Phys. Rev. Lett. **103**, 043601 (2009).

[41] N. Kalb, A. Reiserer, S. Ritter, and G. Rempe, Phys. Rev. Lett. **114**, 220501 (2015).

[42] L.-M. Duan, M. D. Lukin, J. I. Cirac, and P. Zoller, Nature (London) **414**, 413 (2001).

[43] See Supplemental Material at http://link.aps.org/supplemental/10.1103/PhysRevLett.129.050503 for more details on experimental setup, spin-wave freezing, phase noise during storage, and remote entangling efficiency.

[44] M. Fleischhauer, A. Imamoglu, and J. P. Marangos, Rev. Mod. Phys. **77**, 633 (2005).

[45] Y. Jiang, J. Rui, X.-H. Bao, and J.-W. Pan, Phys. Rev. A **93**, 063819 (2016).

[46] Y. Yu, P.-F. Sun, Y.-Z. Zhang, B. Bai, Y.-Q. Fang, X.-Y. Luo, Z.-Y. An, J. Li, J. Zhang, F. Xu, X.-H. Bao, and J.-W. Pan, Phys. Rev. Lett. **127**, 160502 (2021).

[47] H. Shibata, K. Shimizu, H. Takesue, and Y. Tokura, Opt. Lett. **40**, 3428 (2015).

[48] P.-F. Sun, Y. Yu, Z.-Y. An, J. Li, C.-W. Yang, X.-H. Bao, and J.-W. Pan, Phys. Rev. Lett. **128**, 060502 (2022).

[49] T. van Leent, M. Bock, F. Fertig, R. Garthoff, S. Eppelt, Y. Zhou, P. Malik, M. Seubert, T. Bauer, W. Rosenfeld, W. Zhang, C. Becher, and H. Weinfurter, arXiv:2111.15526.